Space–time computations of exactly time-periodic flows past hydrofoils

Lotz, Jacob E.; ten Eikelder, Marco F.P.; Akkerman, Ido

DOI
10.1016/j.compfluid.2024.106286

Publication date
2024

Document Version
Final published version

Published in
Computers and Fluids

Computers and Fluids 277 (2024) 106286

Contents lists available at ScienceDirect

Computers and Fluids

journal homepage: www.elsevier.com/locate/compfluid

Space–time computations of exactly time-periodic flows past hydrofoils

Jacob E. Lotz [a,*], Marco F.P. ten Eikelder [b], Ido Akkerman [a]

[a] Delft University of Technology, Department of Mechanical Engineering, P.O. Box 5, 2600 AA Delft, The Netherlands
[b] Institute for Mechanics, Computational Mechanics Group, Technical University of Darmstadt, Franziska-Braun-Straße 7, 64287 Darmstadt, Germany

ARTICLE INFO

Keywords:
Periodic flow
Space–time methods
Isogeometric analysis
Variation multiscale analysis
Large-eddy simulation
Weak boundary conditions

ABSTRACT

The computation of periodic flows is typically conducted over multiple periods. First, a number of periods is used to develop periodic characteristics, and afterwards statistics are collected from averages over multiple periods. As a consequence, it is uncertain whether the numerical results are exactly time-periodic, and additionally, the time domain might be needlessly long. In this article, we circumvent these concerns by using a time-periodic function space. Consequently, the boundary conditions and solutions are exactly periodic. We employ the isogeometric analysis framework to achieve higher-order smoothness in both space and time. The discretization is performed using residual-based variational multiscale modeling and weak boundary conditions are adopted to enhance the accuracy near the moving boundaries of the computational domain. We enforce the time-periodic boundary condition within the isogeometric discretization spaces, which converts the two-dimensional time-dependent problem into a three-dimensional boundary value problem. Furthermore, we determine the boundary velocities of moving hydrofoils directly from the computational mesh and use a conservation methodology for force extraction. Application of the computational setup to heaving and pitching hydrofoils displays very accurate and exactly periodic results for lift and drag.

1. Introduction

Periodic flows are ubiquitous in a large number of industrial applications and natural features. Prototypical examples include the flow around submerged propellers, wind turbines, or rotating flows in turbomachines and engines and the pulsatile flow of blood. Various challenges arise in the design of practical numerical simulations of these flows. On top of the well-known complications centered around the inertia-driven character and the imposition of boundary conditions, the periodic nature adds novel peculiar hurdles. The typical strategy of simulating a periodic flow problem is to perform an unsteady computation in which the flow develops periodic characteristics [1–3]. As such, the computations are usually not exactly periodic, and the temporal range may be excessively long. Moreover, a user-defined criterion of the characteristics of the flow is inevitable and the flow is never strictly periodic. In this work we exploit the periodic nature of the problem and use a space–time finite element method in the framework of residual-based variational multiscale (VMS) methods, isogeometric analysis and weak boundary conditions. Particular emphasis is on the application to heaving and pitching hydrofoils.

The concept of *space–time finite elements* may be traced back to the late sixties, with contributions by Fried [4] and Oden [5,6] on the generation of finite element models in the time domain. In time-dependent problems, the standard is to separate the discretization of the time (e.g. finite difference schemes) and space (e.g. Galerkin methods). This is often referred to as the *semi-discrete* method. The idea of space–time finite element methods is to adopt the variational approach in the space–time setting such as in [7], where the space–time formulation is used in conjunction with the Galerkin/Least-squares stabilization. This allowed space–time computations for three-dimensional compressible and incompressible flows [8,9]. Contributions to accuracy and stability, along with the use of Fourier-analysis, include the stabilized methods in the space–time framework for the advection–diffusion equation and Navier–Stokes equation [10–12]. This space–time framework was originally formulated for stationary problems and is extended to domains with moving boundaries by Tezduyar and collaborators [13,14]. Space–time computations of 2D time-periodic flows around fixed, oscillating, and bobbing hydrofoils were extensively covered in [1,15,16]. These were the first space–time computations of their kind. A few years later, the *VMS framework* [17,18], encompassing many existing stabilized methods, was proposed. The framework was originally introduced for stationary problems. In [19] it was argued that the most theoretically coherent framework for the extension to time-dependent problems is the space–time context. The most popular applications of the VMS methodology for time-dependent problems are however in the semi-discrete setting. A notable contribution in this regard is

* Corresponding author.
E-mail addresses: j.e.lotz@tudelft.nl (J.E. Lotz), marco.eikelder@tu-darmstadt.de (M.F.P. ten Eikelder), i.akkerman@tudelft.nl (I. Akkerman).

https://doi.org/10.1016/j.compfluid.2024.106286
Received 2 November 2022; Received in revised form 16 January 2024; Accepted 29 April 2024
Available online 3 May 2024

the work [20] that presented a variationally consistent VMS methodology for turbulent flows called *residual-based variational multiscale* (RBVMS). This method is often used in combination with weak boundary conditions [21]. Recently, the popular Nitsche's method for the imposition of weak boundary conditions has been identified as a variational multiscale formulation [22]. The RBVMS method opened the door for the development of a novel class of small-scale models for large-eddy simulations, including dynamic small-scales [23–25] and discontinuity capturing [26,27]. The last important development with implications for the space–time framework that we succinctly discuss, is the introduction of isogeometric analysis [28,29]. In contrast to classical space-finite element methods, isogeometric analysis offers the possibility of arbitrary smooth finite element basis functions. This technique was initially adopted for spatial discretizations, yet it offers rich opportunities in the space–time setting [30–33]. On top of the more widely known advantages of isogeometric analysis, as pointed out as early as in 2012 [34–36], the adoption of it in the space–time context is particularly beneficial for an accurate representation of moving boundaries and a higher continuity in the temporal direction. A good overview of the history and the wide variety of applications of the space–time method can be found in [37], including simulations with isogeometric analysis [38] and RBVMS discretization [34].

The existing space–time finite element methods form a versatile and fundamental class of methodologies for time-dependent problems in fluid mechanics. The space–time method can be adopted for the computation of periodic flows, for example in [1,15,16]. However, just as in the semi-discrete setting, such computations require a transient until a near-periodic state is reached. The numerical results are not strictly periodic. In this article, we circumvent these concerns by performing computations with exact time-periodicity. We compute the periodic state via enforcing the periodicity as a boundary condition in time, see also [39,40]. This turns the two-dimensional time-dependent model into a three-dimensional boundary value problem. Our numerical results show the exact periodicity without losing the expected accuracy in the solutions. To this purpose we adopt a periodic space–time model of arbitrary continuity via isogeometric analysis. Furthermore, we combine this with the usage of the RBVMS methodology and weak boundary conditions, providing a robust periodic space–time method. We show conservation properties of the proposed method and present a conservative traction evaluation. Last, we introduce mesh constraint boundary velocities. We use our computational setup for the simulation of incompressible flow past a prescribed periodically moving hydrofoil.

The paper is organized as follows. We describe the time-periodic continuous space–time setup in Section 2, which fits within the more general space–time framework. Next, in Section 3 we discuss the conservation properties and the continuous force extraction method. In Section 4 we provide results of numerical experiments considering the mesh-constraint boundary velocity, force extraction, and periodic flow. The numerical experiments employ two spatial dimensions. We close with concluding remarks in Section 5.

2. Periodic space–time formulation of the incompressible flow equations

2.1. Governing equations

Consider a time-dependent spatial domain $\Omega = \Omega(t) \subset \mathbb{R}^d$ with boundary $\Gamma = \Gamma_{\text{int}} \cup \Gamma_{\text{ext}}$ composed of a time-dependent interior $\Gamma_{\text{int}} = \Gamma_{\text{int}}(t)$ and exterior part Γ_{ext}. The outward unit normal to the boundary Γ is defined as $\mathbf{n}$. Let us now consider a velocity field $\mathbf{u}$ and introduce the normal velocity $u_n = \mathbf{u}\cdot\mathbf{n}$ with positive and negative parts $u_n^{\pm} = \frac{1}{2}(u_n \pm |u_n|)$. We partition the exterior boundary into an inflow and outflow part according to the definitions:

$$\Gamma_{\text{ext}}^D := \left\{\mathbf{x} \in \Gamma | u_{\text{n}}(\mathbf{x}) < 0\right\}, \tag{1a}$$

$$\Gamma_{\text{ext}}^N := \left\{\mathbf{x} \in \Gamma | u_{\text{n}}(\mathbf{x}) \geq 0\right\}. \tag{1b}$$

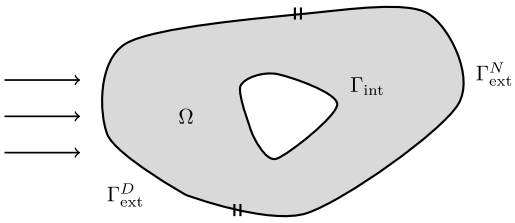

Fig. 1. Sketch of the spatial domain with its boundaries, with inflow on the left.

The domain is depicted in Fig. 1.

We now consider the problem that reads in strong form:

$$\partial_t \mathbf{u} + \mathbf{u}\cdot\nabla\mathbf{u} + \nabla p - \nabla\cdot(2\nu\nabla^s\mathbf{u}) = \mathbf{f} \quad \text{in} \quad \Omega, \tag{2a}$$

$$\nabla\cdot\mathbf{u} = 0 \quad \text{in} \quad \Omega, \tag{2b}$$

$$\mathbf{u} = \mathbf{g}_{\text{int}} \quad \text{in} \quad \Gamma_{\text{int}}, \tag{2c}$$

$$\mathbf{u} = \mathbf{g}_{\text{ext}} \quad \text{in} \quad \Gamma_{\text{ext}}^D, \tag{2d}$$

$$-p\mathbf{n} + \nu\nabla\mathbf{u}\cdot\mathbf{n} + u_{\text{n}}^{-}\mathbf{u} = \mathbf{0} \quad \text{in} \quad \Gamma_{\text{ext}}^N, \tag{2e}$$

$$\mathbf{u}(\cdot,0) = \mathbf{u}_0 \quad \text{in} \quad \Omega. \tag{2f}$$

Here the unknown fields are the velocity $\mathbf{u} = \mathbf{u}(\mathbf{x},t)$ and the pressure $p = p(\mathbf{x},t)$ with spatial coordinate $\mathbf{x}$ and the time coordinate $t \in \mathcal{I} = (0,T)$ with final time $T > 0$. We employ the standard notation for the gradient (∇), the symmetric gradient (∇^s) and the divergence ($\nabla\cdot$). Furthermore, ν denotes the (constant) kinematic viscosity, $\mathbf{f} = \mathbf{f}(t)$ is a (time-dependent) external force, and $\mathbf{g}_{\text{int}} = \mathbf{g}_{\text{int}}(t)$ and $\mathbf{g}_{\text{ext}}$ are prescribed (time-dependent) velocities on the interior boundary and inflow partition of the exterior boundary, respectively. We split the prescribed no-slip velocity into a normal ($\mathbf{g}_n$) and tangential component ($\mathbf{g}_t$):

$$\mathbf{g}_{\text{int}} = \mathbf{g}_n + \mathbf{g}_t, \tag{3a}$$

$$\mathbf{g}_n = (\mathbf{g}_{\text{int}}\cdot\mathbf{n})\mathbf{n}, \tag{3b}$$

$$\mathbf{g}_t\cdot\mathbf{n} = 0. \tag{3c}$$

Denoting the normal velocity of the domain boundary Γ_{int} by $v_n = \mathbf{g}_n\cdot\mathbf{n}$, the normal component $\mathbf{g}_n$ is prescribed by the relation $\mathbf{g}_n = v_n\mathbf{n}$.

The Eqs. (2) describe the incompressible Navier–Stokes equations, with the balance of linear momentum and the continuity equation in (2a) and (2b), the Dirichlet boundary conditions on the interior and the inflow boundary in (2c) and (2d), the outflow boundary condition in (2e) and the initial condition in (2f).

2.2. Space–time formulation

We introduce the (continuous) space–time domain $Q = \Omega\times\mathcal{I}$ as an extrusion of the spatial domain $\Omega = \Omega(t)$. The boundary of Q consists of an interior part $P_{\text{int}} = P_{\text{int}}(t) = \Gamma_{\text{int}}(t)\times\mathcal{I}$, and an exterior part made up of an inflow $P_{\text{ext}}^D = \Gamma_{\text{ext}}^D\times\mathcal{I}$ and an outflow $P_{\text{ext}}^N = \Gamma_{\text{ext}}^N\times\mathcal{I}$ contribution. We visualize the setup in Fig. 2.

We introduce the space–time coordinate $\hat{\mathbf{x}} = [\mathbf{x}^T\ st]^T = [x_1\ \dots\ x_d\ sx_{d+1}]$ and the extended velocity vector $\hat{\mathbf{u}} = [\mathbf{u}^T\ s]^T$, where s is a velocity relating the time and space dimensions. For simplicity, s can be chosen as 1.

In this work we focus on periodic flows and as such, we consider a periodically changing domain Ω with period $\mathcal{T}$:

$$\Omega|_t = \Omega|_{t+\mathcal{T}}. \tag{4}$$

Additionally, we require the prescribed external force $\mathbf{f}$ and boundary velocities to be periodic:

$$\mathbf{f}(\mathbf{x},t) = \mathbf{f}(\mathbf{x},t+\mathcal{T}), \tag{5a}$$

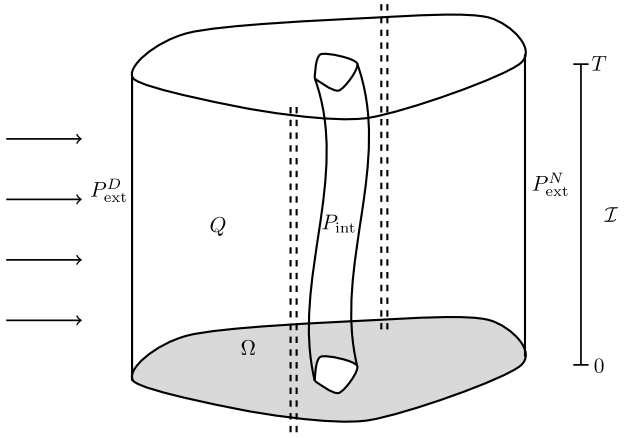

Fig. 2. Sketch of the space–time domain Q with its boundaries P, with inflow on the left, as an extrusion of the spatial domain Ω in gray.

$$\mathbf{g}(\mathbf{x}, t) = \mathbf{g}(\mathbf{x}, t + \mathcal{T}). \tag{5b}$$

The initial condition in (2f) is represented in the space–time setting by the time-periodic condition:

$$\mathbf{u}(\cdot, 0) = \mathbf{u}(\cdot, \mathcal{T}) \quad \text{in} \quad \Omega. \tag{6}$$

We take the final time as $T = \mathcal{T}$ to cover one period.

Using these definitions, problem (2) transforms in the space–time context into the steady state problem:

$$\hat{\mathbf{u}} \cdot \nabla_{\hat{\mathbf{x}}} \mathbf{u} + \nabla p - \nu \nabla^2 \mathbf{u} = \mathbf{f} \quad \text{in} \quad Q, \tag{7a}$$

$$\nabla \cdot \mathbf{u} = 0 \quad \text{in} \quad Q, \tag{7b}$$

$$\mathbf{u} = \mathbf{g}_{\text{int}} \quad \text{in} \quad P_{\text{int}}, \tag{7c}$$

$$\mathbf{u} = \mathbf{g}_{\text{ext}} \quad \text{in} \quad P^D_{\text{ext}}, \tag{7d}$$

$$-p\mathbf{n} + \nu \nabla \mathbf{u} \cdot \mathbf{n} + u_{\text{n}}^{-} \mathbf{u} = \mathbf{0} \quad \text{in} \quad P^N_{\text{ext}}, \tag{7e}$$

$$\mathbf{u}(\cdot, 0) = \mathbf{u}(\cdot, T) \quad \text{in} \quad \Omega. \tag{7f}$$

In (7a) we have combined the first two members of (2a) into a single term via the identity:

$$\partial_t \mathbf{u} + \mathbf{u} \cdot \nabla \mathbf{u} = \hat{\mathbf{u}} \cdot \nabla_{\hat{\mathbf{x}}} \mathbf{u}, \tag{8}$$

where $\nabla_{\hat{\mathbf{x}}}$ is the space–time gradient. The normal $\mathbf{n}$ in (7e) is the classical spatial normal and can be extracted from the space–time normal $\hat{\mathbf{n}} = [n_1 \ \dots \ n_d \ n_{d+1}]^T$ via,

$$\mathbf{n} = \frac{1}{\sqrt{n_1^2 + \cdots + n_d^2}} \begin{bmatrix} n_1 \\ \vdots \\ n_d \end{bmatrix}. \tag{9}$$

The space–time outward normal $\hat{\mathbf{n}}$ has unit length in the norm $\|\cdot\|_{G_s}$ defined by

$$\|\hat{\mathbf{n}}\|^2_{G_s} = \hat{\mathbf{n}} \cdot \mathbf{G}_s \hat{\mathbf{n}}, \tag{10}$$

where $\mathbf{G}_s$ is the space–time metric

$$\mathbf{G}_s = \begin{pmatrix} \mathbf{I}_{d\times d} & 0_{1\times d} \\ 0_{d\times 1} & s^2 \end{pmatrix}. \tag{11}$$

Furthermore, the normal velocity v_n is related to the space–time velocity s and the space–time normal $\hat{\mathbf{n}}$ via:

$$v_n = -s \frac{n_{d+1}}{\sqrt{n_1^2 + .. + n_d^2}}. \tag{12}$$

2.3. Weak formulation of the continuous space–time problem

The weak formulation of the continuous space–time problem is stated using the trial and test function spaces $\mathcal{W}_g$ and $\mathcal{W}_0$ respectively. Members of the trial function space $\mathcal{W}_g$ satisfy the non-homogeneous Dirichlet boundary conditions for the velocity on P^D_{ext} whereas elements in the test function space $\mathcal{W}_0$ satisfy the homogeneous Dirichlet boundary conditions on P^D_{ext}. Additionally, members of both spaces satisfy the periodic boundary condition $\mathbf{u}|_{\Omega_0} = \mathbf{u}|_{\Omega_T}$ where, $\Omega_0 = Q|_{t=0}$ and $\Omega_T = Q|_{t=T}$. To enforce the Dirichlet boundary conditions on P_{int} we introduce the subspaces $\mathcal{V}_g \subset \mathcal{W}_g$ and $\mathcal{V}_0 \subset \mathcal{W}_0$, that additionally satisfy non-homogeneous and homogeneous boundary conditions on P_{int}, respectively.

The variational formulation of (7) now reads as:

find $\boldsymbol{U} = \{\mathbf{u}, p\} \in \mathcal{V}_g$ *such that for all* $\boldsymbol{W} = \{\mathbf{w}, q\} \in \mathcal{V}_0$:

$$B_{\text{GAL}}(\boldsymbol{U}, \boldsymbol{W}) = L(\boldsymbol{W}), \tag{13a}$$

where

$$\begin{aligned} B_{\text{GAL}}(\boldsymbol{U}, \boldsymbol{W}) = &\left(\mathbf{w}, \hat{\mathbf{u}} \cdot \nabla_{\hat{\mathbf{x}}} \mathbf{u}\right)_Q - (\nabla \cdot \mathbf{w}, p)_Q \\ &+ (\nabla \mathbf{w}, \nu \nabla \mathbf{u})_Q + (q, \nabla \cdot \mathbf{u})_Q - \left(\mathbf{w}, u_{\text{n}}^{-} \mathbf{u}\right)_{P^N_{\text{ext}}}, \end{aligned} \tag{13b}$$

$$L(\boldsymbol{W}) = (\mathbf{w}, \mathbf{f})_Q. \tag{13c}$$

The L^2 inner product over D is defined as $(\cdot, \cdot)_D$.

2.4. Weak formulation of the discrete problem

To introduce the numerical discretization, we first subdivide our physical domain Q into elements Q_K. The domain of element interiors denotes:

$$\tilde{Q} = \bigcup_K Q_K. \tag{14}$$

We apply residual-based variational multiscale turbulence modeling [20,41] in which the weighting function space and trial solution space are decomposed into subspaces that contain the coarse and fine scales:

$$\mathcal{W}_g = \mathcal{W}_g^h \oplus \mathcal{W}', \tag{15a}$$

$$\mathcal{W}_0 = \mathcal{W}_0^h \oplus \mathcal{W}', \tag{15b}$$

where $\mathcal{W}_g^h$ and $\mathcal{W}_0^h$ are coarse-scale spaces, and $\mathcal{W}' \subset \mathcal{W}_g \cup \mathcal{W}_0$ are the fine scales. The coarse-scale space is spanned by the finite-dimensional numerical discretization whereas the fine-scales are their infinite-dimensional complement. Uniqueness of the multi-scale split (15) is ensured when the split is established via a projection operator. (15) implies that the members of $\mathcal{W}_g$ and $\mathcal{W}_0$ split as:

$$\{\mathbf{u}, p\} = \left\{\mathbf{u}^h, p^h\right\} + \left\{\mathbf{u}', p'\right\}, \tag{16a}$$

$$\{\mathbf{w}, q\} = \left\{\mathbf{w}^h, q^h\right\} + \left\{\mathbf{w}', q'\right\}, \tag{16b}$$

where the components of the coarse-scale subspaces are denoted as $\boldsymbol{U}^h = \left\{\mathbf{u}^h, p^h\right\} \in \mathcal{W}_g^h$ and $\boldsymbol{W}^h = \left\{\mathbf{w}^h, q^h\right\} \in \mathcal{W}_0^h$, and the components of the small-scale subspace are denoted as $\boldsymbol{U}' = \left\{\mathbf{u}', p'\right\} \in \mathcal{W}'$ and $\boldsymbol{W}' = \left\{\mathbf{w}', q'\right\} \in \mathcal{W}'$.

To arrive at the fully-discrete formulation we make the following modeling choices. First, we apply a pseudo-transient continuation to march in pseudo-time to the space–time steady state solution. Next, we select a standard H^1_0-multiscale projector that eliminates the fine-scale viscosity contribution. Next, we replace the small-scale space $\mathcal{W}'$ with the velocity–pressure product $\mathcal{V}' \times \mathcal{P}'$. The fine-scales are modeled as:

$$\mathbf{u}' = -\tau_M \mathbf{r}_M, \tag{17a}$$

$$p' = -\tau_C r_C, \tag{17b}$$

with the strong residuals

$$\mathbf{r}_M = \left(\hat{\mathbf{u}}^h \cdot \nabla_{\hat{\mathbf{x}}}\right) \mathbf{u}^h - \nabla p - \nu \nabla^2 \mathbf{u}^h - \mathbf{f}, \tag{18a}$$

$$r_C = \nabla \cdot \mathbf{u}^h, \tag{18b}$$

and stability parameters

$$\tau_M = \left(\hat{\mathbf{u}}^h \cdot \hat{\mathbf{G}}\hat{\mathbf{u}}^h + C^I \nu^2 \mathbf{G} : \mathbf{G}\right)^{-1/2}, \tag{19a}$$

$$\tau_C = \tau_M^{-1} \mathrm{Tr}(\mathbf{G})^{-1}. \tag{19b}$$

In both the momentum residual and its corresponding stability parameter the time derivative is incorporated in the convection term, analogous to (8). As a consequence, the convective and diffusive contributions depend on two different metric tensors, the space–time metric tensor $\hat{\mathbf{G}}$ and spatial metric tensor $\mathbf{G}$, respectively. These metric tensors are given by

$$\hat{\mathbf{G}} = \left(\frac{\partial \boldsymbol{\xi}}{\partial \hat{\mathbf{x}}}\right)^T \mathbf{G}_s \frac{\partial \boldsymbol{\xi}}{\partial \hat{\mathbf{x}}}, \qquad \mathbf{G} = \left(\frac{\partial \boldsymbol{\xi}}{\partial \mathbf{x}}\right)^T \frac{\partial \boldsymbol{\xi}}{\partial \mathbf{x}}. \tag{20}$$

Lastly, we enforce the Dirichlet boundary conditions weakly [21]. To this purpose we introduce the penalty parameter

$$\tau_b = \frac{1}{2} C_b^I \nu \left(\mathbf{n} \cdot \mathbf{G}\mathbf{n}\right)^{\frac{1}{2}}. \tag{21}$$

We now define the fully-discrete time-periodic formulation. The formulation fits within the well-known space–time framework. In particular, as a consequence of the continuous spaces, the jump term across the space–time slabs that is common in the space–time method is absent. The method reads as:

find $\boldsymbol{U}^h = \{\mathbf{u}^h, p^h\} \in \mathcal{W}_g^h$ *such that for all* $\boldsymbol{W} = \{\mathbf{w}^h, q^h\} \in \mathcal{W}_0^h$*:*

$$B\left(\boldsymbol{U}^h, \boldsymbol{W}^h\right) = L\left(\boldsymbol{W}^h\right), \tag{22a}$$

where

$$\begin{aligned} B\left(\boldsymbol{U}^h, \boldsymbol{W}^h\right) = {} & B_{\mathrm{GAL}}\left(\boldsymbol{U}^h, \boldsymbol{W}^h\right) + B_{\mathrm{PT}}\left(\boldsymbol{U}^h, \boldsymbol{W}^h\right) \\ & + B_{\mathrm{STAB}}\left(\boldsymbol{U}^h, \boldsymbol{W}^h\right) + B_{\mathrm{WBC}}\left(\boldsymbol{U}^h, \boldsymbol{W}^h\right), \end{aligned} \tag{22b}$$

$$B_{\mathrm{PT}}\left(\boldsymbol{U}^h, \boldsymbol{W}^h\right) = \left(\mathbf{w}^h, \partial_\theta \mathbf{u}^h\right)_Q + \frac{1}{a^2}\left(q^h, \partial_\theta p^h\right)_Q, \tag{22c}$$

$$\begin{aligned} B_{\mathrm{STAB}}\left(\boldsymbol{U}^h, \boldsymbol{W}^h\right) = {} & -\left(\nabla_{\hat{\mathbf{x}}} \mathbf{w}^h, \mathbf{u}' \otimes \hat{\mathbf{u}}^h\right)_{\tilde{Q}} - \left(\nabla \mathbf{w}^h, \mathbf{u}^h \otimes \mathbf{u}'\right)_{\tilde{Q}} \\ & - \left(\nabla \mathbf{w}^h, \mathbf{u}' \otimes \mathbf{u}'\right)_{\tilde{Q}} - \left(\nabla q^h, \mathbf{u}'\right)_{\tilde{Q}} - \left(\nabla \cdot \mathbf{w}^h, p'\right)_{\tilde{Q}}, \end{aligned} \tag{22d}$$

$$\begin{aligned} B_{\mathrm{WBC}}\left(\boldsymbol{U}^h, \boldsymbol{W}^h\right) = {} & \left(\mathbf{w}^h, p^h\mathbf{n} - \nu \nabla \mathbf{u}^h \cdot \mathbf{n}\right)_{P_{\mathrm{int}}} + \left(\nu \nabla \mathbf{w}^h \cdot \mathbf{n} - q^h \mathbf{n}, \mathbf{u}^h - \mathbf{g}\right)_{P_{\mathrm{int}}} \\ & + \left(\mathbf{w}^h \tau_b, \mathbf{u}^h - \mathbf{g}\right)_{P_{\mathrm{int}}}. \end{aligned} \tag{22e}$$

Eq. (22c) represents the pseudo-transient continuation as a globalization technique [42,43]. The pseudo-transient continuation technique is a widely applied methodology that obtains the steady state solution by adding a derivative to pseudo-time θ. The first term is classical, whereas the utilization of the second term is non-standard. This term introduces artificial compressibility [44–46], where a is an artificial speed of sound. This term overcomes some of the difficulties due to the saddle-point nature of the underlying problem (i.e. the absence of a pressure term in the continuity equation). Moreover, we note the introduction of this term permits more powerful preconditioning options such as algebraic multigrid (AMG). We remark that the numerical solution of the problem is fully incompressible and thus does not depend on the artificial speed of sound a.

Eq. (22d) describes terms associated with variational multiscale stabilization [20]. In LES terminology the first two terms represent the cross-stress, while the third term represents the Reynolds stress. In the context of stabilized methods, the first term is the Streamline-upwind Petrov–Galerkin (SUPG) term [47], and the fourth and last terms are the Pressure-Stabilizing/Petrov–Galerkin (PSPG) [48] and Least-Squares on Incompressibility Constraint (LSIC) terms respectively. Note that the first and the second terms are not each other transposes. Namely, we incorporate the temporal derivative of the fine-scales in the SUPG term:

$$\left(\mathbf{w}, \partial_t \mathbf{u}'\right)_{\tilde{Q}} + \left(\nabla \mathbf{w}^h, \mathbf{u}' \otimes \mathbf{u}^h\right)_{\tilde{Q}} = \left(\nabla_{\hat{\mathbf{x}}} \mathbf{w}^h, \mathbf{u}' \otimes \hat{\mathbf{u}}^h\right)_{\tilde{Q}}. \tag{23}$$

This relation is a direct consequence of the partial integration (in the temporal direction) of the fine-scale time-derivative term:

$$\left(\mathbf{w}, \partial_t \mathbf{u}'\right)_{\tilde{Q}} = -\left(\partial_t \mathbf{w}, \mathbf{u}'\right)_{\tilde{Q}}, \tag{24}$$

where we note the absence of boundary contributions due to the periodic boundary conditions.

Lastly, Eq. (22e) enforces the weak boundary conditions on the interior boundary (7c). The first term is the consistency term. This term originates from integration by parts and as such guarantees variational consistency. The second term is the so-called the dual consistency term, and the last term is the penalty term that ensures the stability of the formulation. We recall that the Dirichlet boundary conditions in (7d) on P_{ext}^D are enforced strongly.

3. Conservation properties

In this section we establish the conservation properties of the discrete method. We show conservation of mass, conservation of linear momentum and provide an approach to conservatively evaluate the traction. We consider a converged solution where $\partial_\theta \mathbf{u}^h = \partial_\theta p^h = 0$.

3.1. Conservation of mass

The global conservation of mass directly follows by selecting the weighting function $\boldsymbol{W}^h = \{\mathbf{0}, 1\}$ in the discrete weak formulation (22):

$$\int_Q \nabla \cdot \mathbf{u}^h \, \mathrm{d}x = 0. \tag{25}$$

We do not attain conservation of mass per time-slab since the weighting function with pressure component that equals 1 on a single time-slab and 0 on the others is not a member of $\mathcal{W}_0^h$. Remark that it is possible to work with a particular selection of isogeometric velocity–pressure spaces that establishes pointwise satisfaction of the incompressibility constraint [24,49].

3.2. Conservation of linear momentum

In order to study the conservation of linear momentum one might wish to substitute the weighting function $\boldsymbol{W}^h = \{\mathbf{w}^h, q^h\} = \{\mathbf{e}_i, 0\}$ with $\mathbf{e}_i \in \mathbb{R}^d$ the ith Cartesian unit vector into the discrete weak formulation (22). This choice is not permitted: $\{\mathbf{e}_i, 0\} \notin \mathcal{W}_0^h$. One possible remedy is to work with unconstrained function spaces and weakly enforce the non-homogeneous boundary condition via a Lagrange multiplier construct [24,50]. The Lagrange multiplier is also called *auxiliary flux* [51] and is used to show global and local conservation. The method yields conservative boundary fluxes which is a major advantage as compared to utilizing direct procedures that provide non-conservative boundary fluxes.

We denote the vector-valued Lagrange multiplier/auxiliary flux as λ. Recall that the discrete weak formulation (22) is defined for the test function space $\mathcal{W}_0^h$ in which the velocity test functions vanish on P_{ext}^D. In order to present the augmented formulation, we require the introduction of other test function spaces. Denote the set of all velocity basis functions η and, furthermore, denote with η_g the set of velocity basis functions that do not vanish on P_{ext}^D. With the notation $\mathcal{W}_0^h = \mathcal{U}_0^h \times \mathcal{P}^h$ of the velocity and pressure components of the test function space, we have $\mathcal{U}_0^h = \mathrm{span}\left\{\boldsymbol{N}_A\right\}_{A \in \eta - \eta_g}$, where $\boldsymbol{N}_A = \boldsymbol{N}_A(\boldsymbol{x})$ are the

velocity basis functions. Furthermore, we introduce the unrestricted velocity space $\mathcal{U}^h = \text{span}\left\{\boldsymbol{N}_A\right\}_{A\in\eta}$ and unrestricted velocity–pressure space $\mathcal{W}^h = \mathcal{U}^h \times \mathcal{P}^h$. The augmented problem now reads:

find $\boldsymbol{U}^h \in \mathcal{W}_g^h$ *such that for all* $\bar{\boldsymbol{W}}^h = \left\{\bar{\mathbf{w}}^h, q^h\right\} \in \mathcal{W}^h$*:*

$$(\lambda^h, \bar{\mathbf{w}}^h)_{P_{\text{ext}}^D} = B\left(\boldsymbol{U}^h, \bar{\boldsymbol{W}}^h\right) - L\left(\bar{\boldsymbol{W}}^h\right). \tag{26}$$

This problem splits as:

find $\boldsymbol{U}^h \in \mathcal{W}_g^h$ *and* $\lambda^h \in \mathcal{W}^h - \mathcal{W}_0^h$ *such that*

$$0 = B\left(\boldsymbol{U}^h, \boldsymbol{W}^h\right) - L\left(\boldsymbol{W}^h\right) \quad \text{for all} \quad \boldsymbol{W}^h \in \mathcal{W}_0^h \tag{27a}$$

$$(\lambda^h, \bar{\mathbf{w}}^h)_{P_{\text{ext}}^D} = B\left(\boldsymbol{U}^h, \bar{\boldsymbol{W}}^h\right) - L\left(\bar{\boldsymbol{W}}^h\right) \quad \text{for all} \quad \bar{\boldsymbol{W}}^h \in \mathcal{W}^h - \mathcal{W}_0^h. \tag{27b}$$

The first subproblem coincides with our original weak formulation and thus completely determines the numerical solution $\boldsymbol{U}^h \in \mathcal{W}_g^h$. This solution may be directly substituted into the second subproblem to evaluate the discrete auxiliary flux $\lambda^h \in \mathcal{W}^h - \mathcal{W}_0^h$.

We are now in the position to evaluate the linear momentum conservation and select $\bar{\boldsymbol{W}}^h = \left\{\mathbf{e}_i, 0\right\}$ in (26):

$$\int_{P_{\text{ext}}^D} \lambda_i^h \, \mathrm{d}s = \int_{P_{\text{int}}} p^h n_i - \nu(u_{i,j} + u_{j,i}) n_j \, \mathrm{d}s - \int_Q f_i \, \mathrm{d}x \tag{28}$$

$$- \int_{P_{\text{ext}}^N} u_{\text{n}}^- u_i^h \, \mathrm{d}s + \int_{P_{\text{int}}} \tau_b (u_i^h - g_i) \, \mathrm{d}s. \tag{29}$$

This shows that λ_i^h represents the total conserved boundary flux on P_{ext}^D. Remark that the last two members on the right-hand side result from the usage of weak boundary conditions on P_{int} and are thus absent when instead imposing these conditions strongly.

3.3. Conservative traction evaluation

With the aim of evaluating the time-dependent traction on the interior boundary Γ_{int} we select $\bar{\boldsymbol{W}}^h = \left\{\mathbf{e}_i N_a, 0\right\}$ in (26) with $N_a = N_a(t)$ an arbitrary basis function in the temporal direction. Note that this choice is permitted due to the tensor structure of the NURBS computational mesh. Substitution provides:

$$\begin{aligned}
&\int_{P_{\text{ext}}^D} \lambda_i^h N_a \, \mathrm{d}s + \int_Q f_i N_a \, \mathrm{d}x + \int_{P_{\text{ext}}^N} u_{\text{n}}^- u_i^h \, N_a \, \mathrm{d}s \\
&= \int_{P_{\text{int}}} p^h n_i N_a - \nu(u_{i,j} + u_{j,i}) n_j N_a \, \mathrm{d}s \\
&+ \int_{P_{\text{int}}} \tau_b (u_i^h - g_i) N_a \, \mathrm{d}s.
\end{aligned} \tag{30}$$

The right-hand side of (30) contains all the integrals on the interior boundary P_{int}. In order to evaluate the (vector-valued) traction force $\boldsymbol{\psi}$ we introduce the discrete problems for $i = 1, \ \ldots, \ d$:

find $\psi_i^h \in \text{span}\left\{N_b\right\}_{b\in\xi}$ *such that*

$$\begin{aligned}
\int_{P_{\text{int}}} \psi_i^h N_a \, \mathrm{d}s = &\int_{P_{\text{int}}} p^h n_i N_a - \nu(u_{i,j} + u_{j,i}) n_j N_a \, \mathrm{d}s \\
&+ \int_{P_{\text{int}}} \tau_b (u_i^h - g_i) N_a \, \mathrm{d}s
\end{aligned} \tag{31}$$

where ξ is the set of basis function numbers in the time direction. The traction forces ψ_i^h thus result from inverting a mass matrix (per direction).

4. Numerical experiments

In this section, we discuss the computational setup and subsequently provide results of four numerical experiments using the formulation in Section 2.4. We evaluate the forces in the space–time domain using the conservative traction evaluation of Section 3.3. First, we compare the results of the mesh-constraint boundary velocity of a sinusoidal heaving hydrofoil with the analytical solution and study its dependency on the temporal discretization. Second, in order to examine the capability of the proposed methodology of predicting steady flow, we study the results of fluid flow past a stationary hydrofoil. We perform a grid convergence study and compare our results with the literature. Third, we focus on the hydrodynamics of a moving body, which is much more complex than the case of a steady body. We simulate the flow past a low-frequency heaving hydrofoil. Lastly, we investigate the predictive capability of the methodology on capturing history effects in the wake. We simulate the flow past a pitching hydrofoil at a moderate frequency. Experimental data considering (unsteady) forces on a hydrofoil in a low Reynolds-number flow is not available in the literature. We support our predictions with numerical results from the literature and steady state simulations using the steady variant of the flow model (22). All results presented here correspond to simulations using two spatial dimensions. The third direction refers to time.

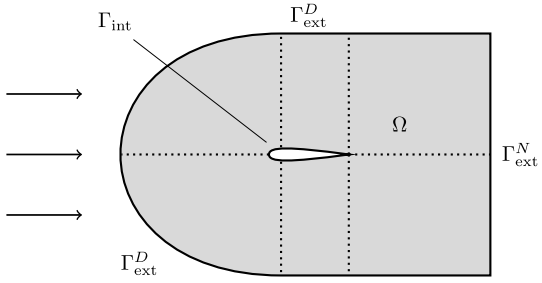

Fig. 3. Schematic representation of the domain Ω, as a time slice of P, surrounding the hydrofoil with the no-slip boundary Γ_{int}, the inflow boundary Γ_{ext}^D and the outflow boundary Γ_{ext}^N. The arrows indicate the direction of the flow. The six NURBS patches are indicated with a dotted line.

4.1. Computational setup

We introduce the space–time domain Q as an extrusion of the spatial domain Ω enclosing a symmetric four-digit NACA foil section [52]. The spatial domain is discretized as a C-shaped mesh using six NURBS patches employing second-order NURBS. The spatial domain is illustrated in Fig. 3. The discretization is C^1-continuous inside the patches and C^0-continuous across patches. The hydrofoil and its motion are incorporated into the space–time mesh using curve interpolation.

Fig. 4 provides an overview and a close-up of a temporal slice of the mesh. The mesh is constructed with the aim of achieving high quality near the hydrofoil. Based on simulations of the flow past a cylinder [53], we choose the distance between Γ_{int} and Γ_{ext} to be 8 chord lengths in order to preclude influence from the outflow boundary Γ_{ext}. We have numerically verified that influence of Γ_{ext} is virtually absent. We select the chord c and free stream velocity U as $c = U = 1$. The numerical experiments are conducted in DelFI, which is based on the MFEM library [54].

The time-marching in pseudo-time θ towards a steady solution typically consists of 14 pseudo-time steps of 5 seconds using the backward Euler method as a pseudo-time marching scheme. As a stopping criterion, we terminate the computation when the L^2-norm of the residual of the momentum and mass equations is smaller than 10^{-6} at the start of the first Newton iteration. Per time step we use 5 Newton iterations. We choose the artificial speed of sound a as 4, which exceeds the velocities encountered in the simulations. This provides a significant reduction in simulation time. Furthermore, we select the inverse estimate coefficients as $C^I = 36$ and $C_b^I = 8$. We note that the latter is only suitable for polynomial degrees up to 2.

Lastly, we discuss the computation of the boundary velocity on the interior boundary $\mathbf{g}_{\text{int}}$. We recall the split:

$$\mathbf{g}_{\text{int}} = \mathbf{g}_n + \mathbf{g}_t, \tag{32a}$$

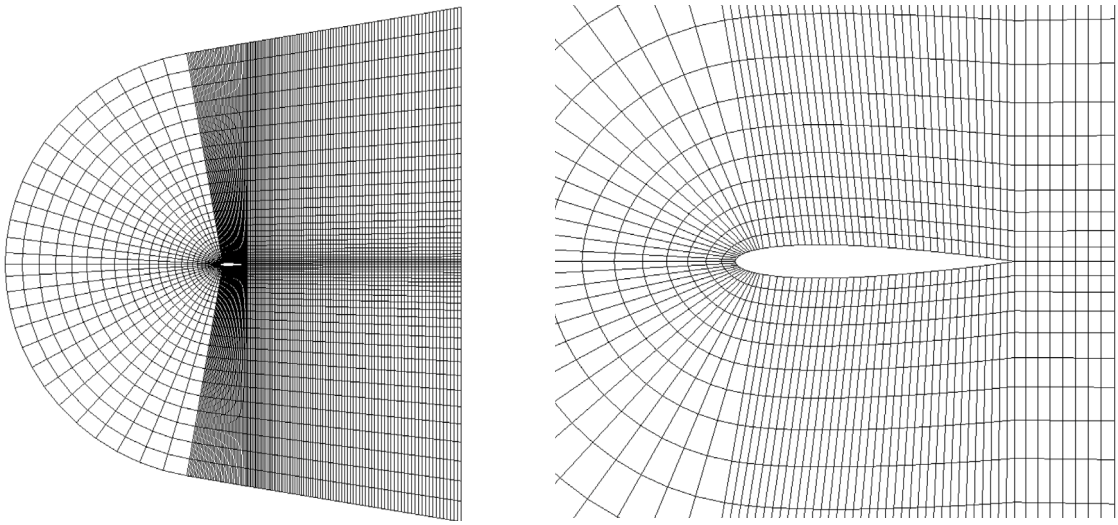

Fig. 4. The spatial mesh as a slice in time: (a) The full C-shaped spatial mesh; (b) A close-up of the spatial mesh near the interpolated hydrofoil.

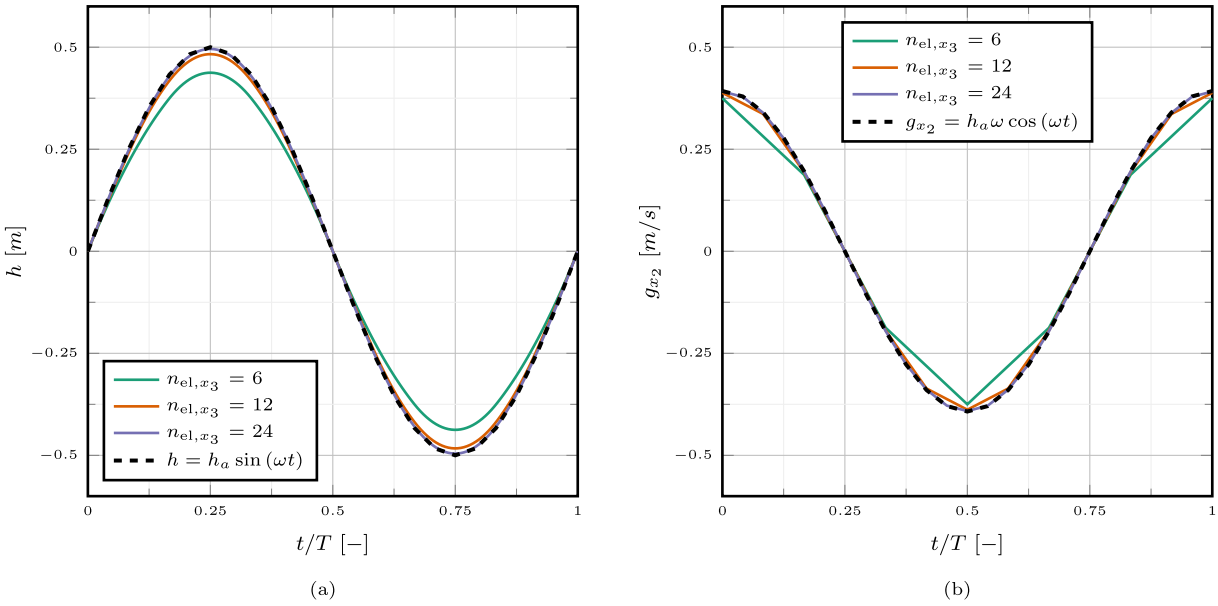

Fig. 5. The motion h in (a) and velocity g_{x_2} in (b) of the hydrofoil in x_2-direction for 3 resolutions n_{el,x_3} in time direction and the analytical solution for a heave motion with $T = 8$ s.

$$\mathbf{g}_n = (\mathbf{g}_{\mathrm{int}} \cdot \mathbf{n})\mathbf{n} = v_n \mathbf{n}, \tag{32b}$$

$$\mathbf{g}_t \cdot \mathbf{n} = 0, \tag{32c}$$

where v_n satisfies the relation (12). The domain motion fully prescribes $\mathbf{g}_n$, while the tangential component $\mathbf{g}_t$ is still undetermined. To numerically determine $\mathbf{g}_{\mathrm{int}}$ however, we use the motion encoded in the mesh and do not rely on the relation (12). The following procedure is permitted due to the extrusion structure of the space–time mesh. We have the following relations:

$$t = t(\xi_{d+1}), \tag{33a}$$

$$\mathbf{X} = \mathbf{X}(\xi_1, \dots \xi_d), \tag{33b}$$

where $\mathbf{X}$ is a Lagrangian coordinate labeling a particle, and where $\boldsymbol{\xi}$ are the coordinates in the reference domain. We compute the boundary velocity by taking the derivative of the spatial coordinate $\mathbf{x}$ to the time direction $t = x_{d+1}$ on a particle path:

$$\mathbf{g}_{\mathrm{int}} = \left.\frac{\partial \mathbf{x}}{\partial t}\right|_{\mathbf{X}} \quad \text{in} \quad P_{\mathrm{int}}. \tag{34}$$

Realizing the dependence $\mathbf{x} = \mathbf{x}(\xi_1, \dots \xi_{d+1})$, we can use the chain rule to conclude:

$$\mathbf{g}_{\mathrm{int}} = s \left.\frac{\partial \mathbf{x}}{\partial x_{d+1}}\right|_{\mathbf{X}} = s \sum_{i=1}^{d+1} \frac{\partial \mathbf{x}}{\partial \xi_i} \left.\frac{\partial \xi_i}{\partial x_{d+1}}\right|_{\mathbf{X}} = s \frac{\partial \mathbf{x}}{\partial \xi_{d+1}} \frac{\partial \xi_{d+1}}{\partial x_{d+1}} \quad \text{in} \quad P_{\mathrm{int}}. \tag{35}$$

We note that the velocity $\mathbf{g}_{\mathrm{int}}$ computed via (35) satisfies $\mathbf{g}_{\mathrm{int}} \cdot \mathbf{n} = v_n$, where v_n is given by (12).

4.2. Mesh-constraint boundary velocity

We evaluate the mesh motion and the resulting mesh-constraint boundary $\mathbf{g}_{\mathrm{int}}$ velocity. We apply a heave motion to the hydrofoil such that it only moves in the x_2-direction. The heave motion of the hydrofoil is sinusoidal with $h(t) = h_a \sin(2\pi t/T)$, with the amplitude

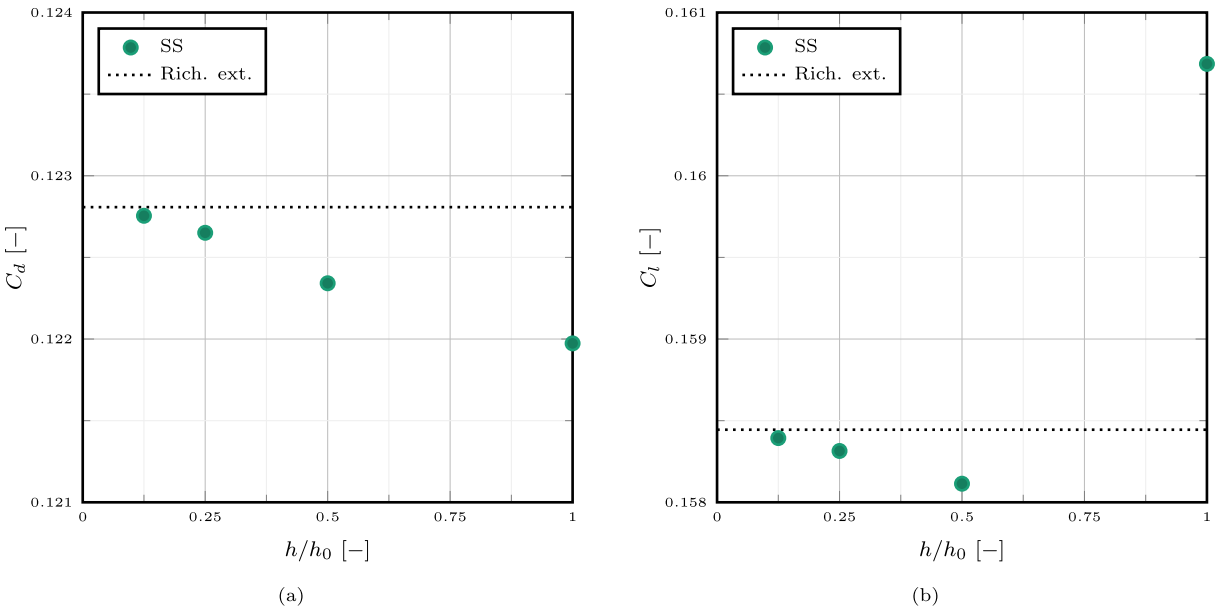

Fig. 6. Results of steady state (SS) simulations for the drag coefficient C_d in (a) and lift coefficient C_l in (b) using four meshes and a Richardson extrapolation of the limit $h/h_0 \to 0$ based on the three fines meshes. The order of convergence is 1.57 and 1.34 for drag and lift respectively.

$h_a = 0.5$ m and the period $T = 8$ s. We use three different temporal resolutions consisting of 6, 12 and 24 elements in the temporal direction n_{el,x_3}.

Fig. 5(a) presents the resulting mesh motion with the corresponding analytical solution. The second-order NURBS are reconstructed using the control points from the mesh. We observe that the finest mesh with $n_{\text{el},x_3} = 24$ is virtually indistinguishable from the analytical solution. Next, we visualize the resulting vertical boundary velocity g_{x_2} and the corresponding analytical solution in Fig. 5(b). The velocities are linear within the element due to the C^1 mesh continuity. Again, the results on the finest mesh with $n_{\text{el},x_3} = 24$ are virtually indistinguishable from the analytical solution.

4.3. Stationary hydrofoil

We simulate the flow past a stationary hydrofoil for angles of attack α ranging from 1° to 5°. The simulations are performed on a NACA0012 foil section with Reynolds number $\mathbb{R}\text{e} = Uc/\nu = 1000$ where ν is the kinematic viscosity. We study the resulting drag coefficient C_d and lift coefficient C_l defined as:

$$C_d = \frac{2F_d}{\rho c U^2}, \tag{36a}$$

$$C_l = \frac{2F_l}{\rho c U^2}, \tag{36b}$$

where F_d is the force component in the flow direction, F_l the force component perpendicular to the flow direction, and ρ denotes the density.

We first consider the steady state setup. Fig. 6 shows the results of the spatial grid convergence study for C_d and C_l using 4 different meshes of varying resolution. In the coarsest mesh the domain is discretized using 30 elements over the length of the hydrofoil, 15 elements between the hydrofoil and the inflow boundary, and 45 elements between the hydrofoil and the outflow boundary. We use a Richardson extrapolation to examine the limit $h/h_0 \to 0$ using the three finest meshes only, as the coarsest mesh is not in the asymptotic range. We find 1.57 and 1.34 for the order of convergence of the drag and lift, respectively. We choose the mesh with two refinements for our computations as this gives a balance between results and computational efforts. For this mesh the error is 0.13% and 0.08% for C_d and C_l respectively considering the extrapolated result for $h/h_0 \to 0$.

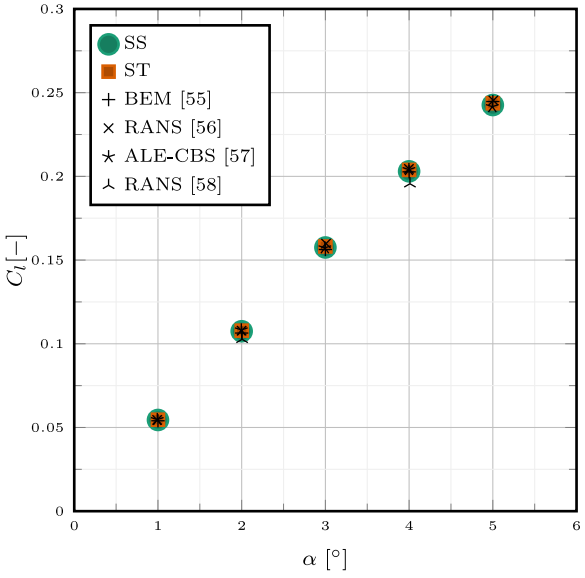

Fig. 7. Lift coefficient C_l at $\mathbb{R}\text{e} = 1000$ of a stationary NACA0012 hydrofoil for several angles of attack α determined using the proposed method and a steady state (SS) solution supplemented with results from the literature.

Next, we focus on the lift coefficient. Fig. 7 shows C_l determined in stationary space–time and steady state simulations, supplemented with results from the literature. The computations are performed for 5 different angles of attack. The similarity of the results of the space–time and steady state simulations demonstrates that the spatial convergence of steady state simulations is indeed sufficient for space–time simulations. Moreover, the results are in good agreement with the results from the literature. We compare with (i) a Boundary Element Method (BEM) with viscous correction XFoil [55], (ii) the Reynolds Averaged Navier Stokes (RANS) solver Ansys Fluent [56], (iii) an Arbitrary-Lagrangian–Eulerian Characteristic Based Split Scheme (ALE-CBS) solver [57], and (iv) other Ansys Fluent computations [58]. The last computations are only available for the angles of attack of 2° and 4°. The numerical results obtained with this solver deviate more from the results that we

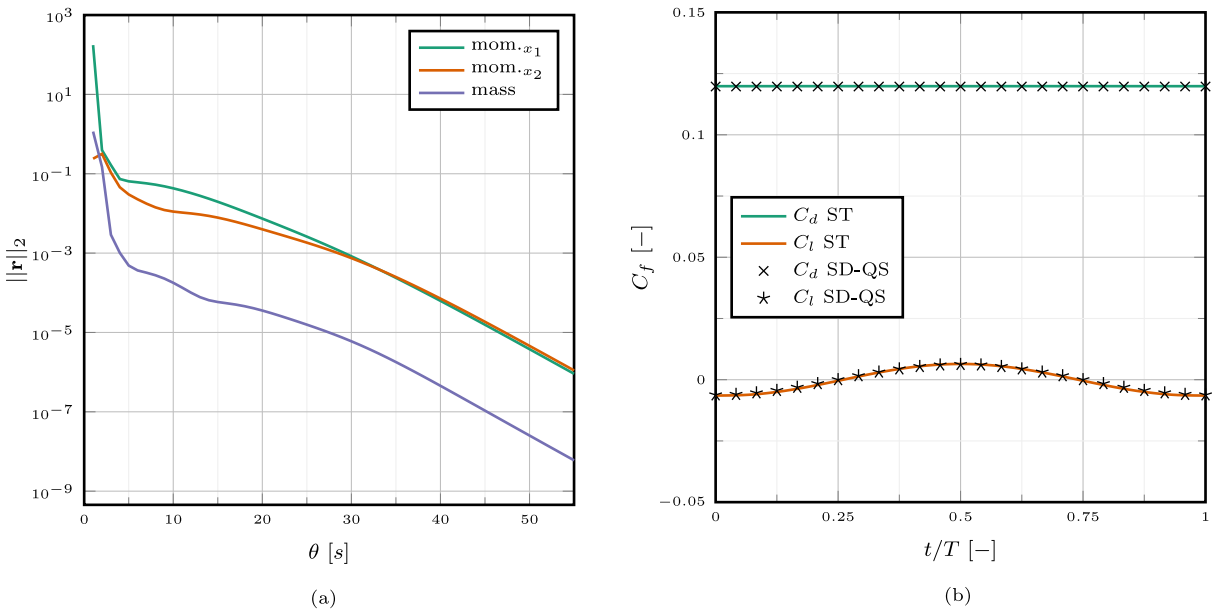

Fig. 8. The convergence and results of the case of a slowly sinusoidal heaving NACA0012 hydrofoil with $k = 0.01$ and $\mathbb{R}\mathrm{e} = 1000$: (a) L^2-norm of the residuals at the start of the first Newton iteration of space–time momentum and mass conservation over pseudo-time θ; (b) Force coefficients $C_f = C_d, C_l$ in space–time (ST) compared to semi-discrete quasi-static (SD-QS) results.

have obtained. Lastly, we note that we have verified the force signal of the space–time simulations to be constant in time. This demonstrates that our method correctly predicts steady flow.

4.4. Heaving hydrofoil at a low reduced frequency

In this test case, we simulate a slowly heaving hydrofoil. The hydrofoil is oscillating at a low reduced frequency $k = \pi c/(TU)$. We note that the effect of the unsteady wake on the flow past the hydrofoil is very low [59] and added mass effects are negligible. As a consequence, the forces on the hydrofoil should match these from quasi-static simulations. We obtain the quasi-static results using stationary steady state simulations where we compensate the angle of attack α for inflow due to the heave motion. This provides the effective angle of attack:

$$\alpha_{\text{eff}} = \alpha - \arctan\left(\frac{2\pi h_a \cos\left(2\pi T^{-1} t\right)}{TU}\right). \tag{37}$$

The simulations are performed with $\mathbb{R}\mathrm{e} = 1000$, $k = 0.01$, $h_a = 0.1$ m and $\alpha = 0°$. We use the same spatial discretization as for the stationary cases. In the temporal direction we use $n_{\text{el},x_3} = 24$. We note that further refinement does not improve the numerical results.

We visualize the convergence of the residuals in Fig. 8(a). We have verified that using stricter convergence criteria does not improve the solution quality. In Fig. 8(b) we show C_l and C_d for the space–time and steady state simulations. We observe that both C_l and C_d agree with the quasi-static results.

4.5. Hydrofoil with large angle pitch motion

In this last, test case we focus on the prediction of the history effects in the wake. We simulate the flow past a sinusoidal pitching NACA0015 hydrofoil. The hydrofoil pitches around the 1/3 chord with motion $\alpha(t) = \alpha_a \sin(2\pi t/T)$, where the amplitude is $\alpha_a = 23°$, the Reynolds number is $\mathbb{R}\mathrm{e} = 1100$ and frequency is $k = 0.377$.

The same case is studied by [3] using Ansys Fluent. Their simulation setup uses an impulsive start and at least 20 large time steps to move the wake downstream of the hydrofoil. Their simulation is pursued with more than 2000 time steps per period. Its result is considered periodic if the maximum variation in mean statistics between the last cycles is 0.1%. In our setup we use the same spatial discretization as in our previous space–time simulations. To accurately capture the flow characteristics, we apply two extra refinements in the temporal direction. We note that further refinement does not yield improved solution quality.

In Fig. 9 we show a time signal of the lift coefficient C_l. In general we observe good agreement between our result and the result of [3]. We see small differences in the regions $0.10 < t/T < 0.43$ and $0.58 < t/T < 0.84$. One important difference between our setup and the simulation in [3] is that our solution is exactly periodic which is not the case in the reference computation. In Fig. 10 we show the velocity and pressure fields for 8 moments in time. Note the periodic solution behavior. This is most apparent in the flow behind the hydrofoil when comparing the velocity field at $t/T = 7/8$ and $t/T = 0$. Furthermore, note that the flow is symmetric around the x-axis. To see this, compare for instance the velocity field at $t/T = 0$ with $t/T = 4/8$ and $t/T = 2/8$ with $t/T = 6/8$. Both figures illustrate that the effect of the history in the wake is correctly predicted.

5. Conclusions

In this work we present a time-periodic continuous space–time computational setup to simulate flow past periodically moving objects. This ensures that the flow is exactly periodic, and precludes working with needlessly long time domains. We enforce the time-periodicity constraint as a boundary condition in time. This changes the time-dependent two-dimensional problem into a three-dimensional boundary value problem in both space and time. The method employs isogeometric analysis to achieve higher-order smoothness in space and time. We discretize the formulation using residual-based variational turbulence modeling in which turbulent eddy viscosities are absent. Furthermore, we use weak boundary conditions to enhance the accuracy near the moving boundaries of the computational domain and pseudo-transient continuation to overcome some of the difficulties related to the saddle-point nature of the underlying problem. We show

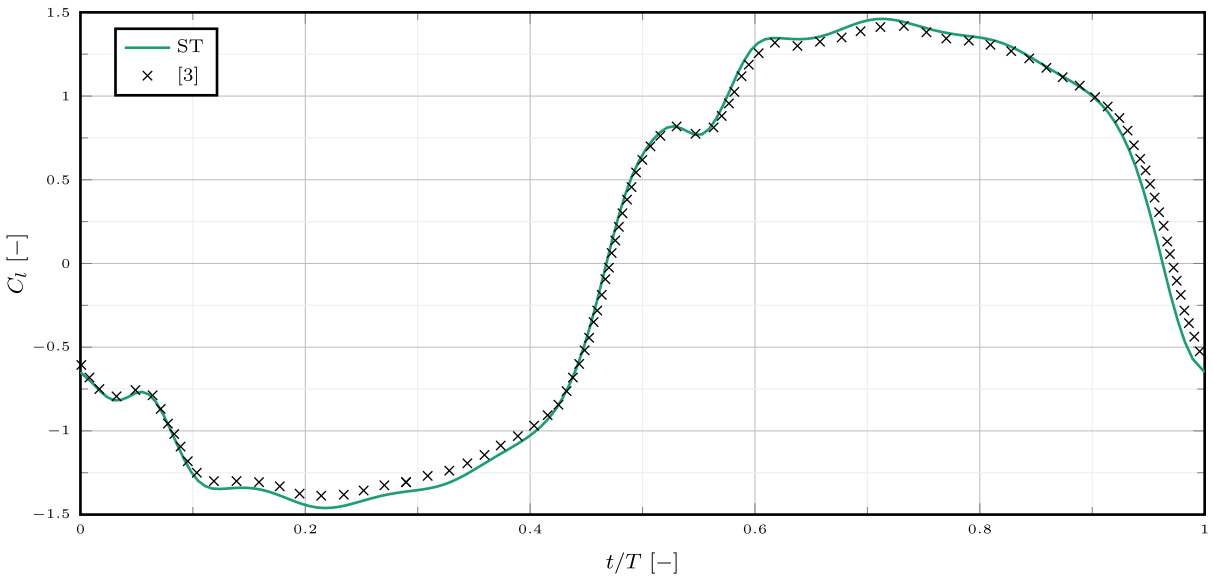

Fig. 9. Lift coefficient C_l over time of a pitching NACA0015 hydrofoil with $\alpha_a = 23°$, l and $\mathbb{R}e = 1100$.

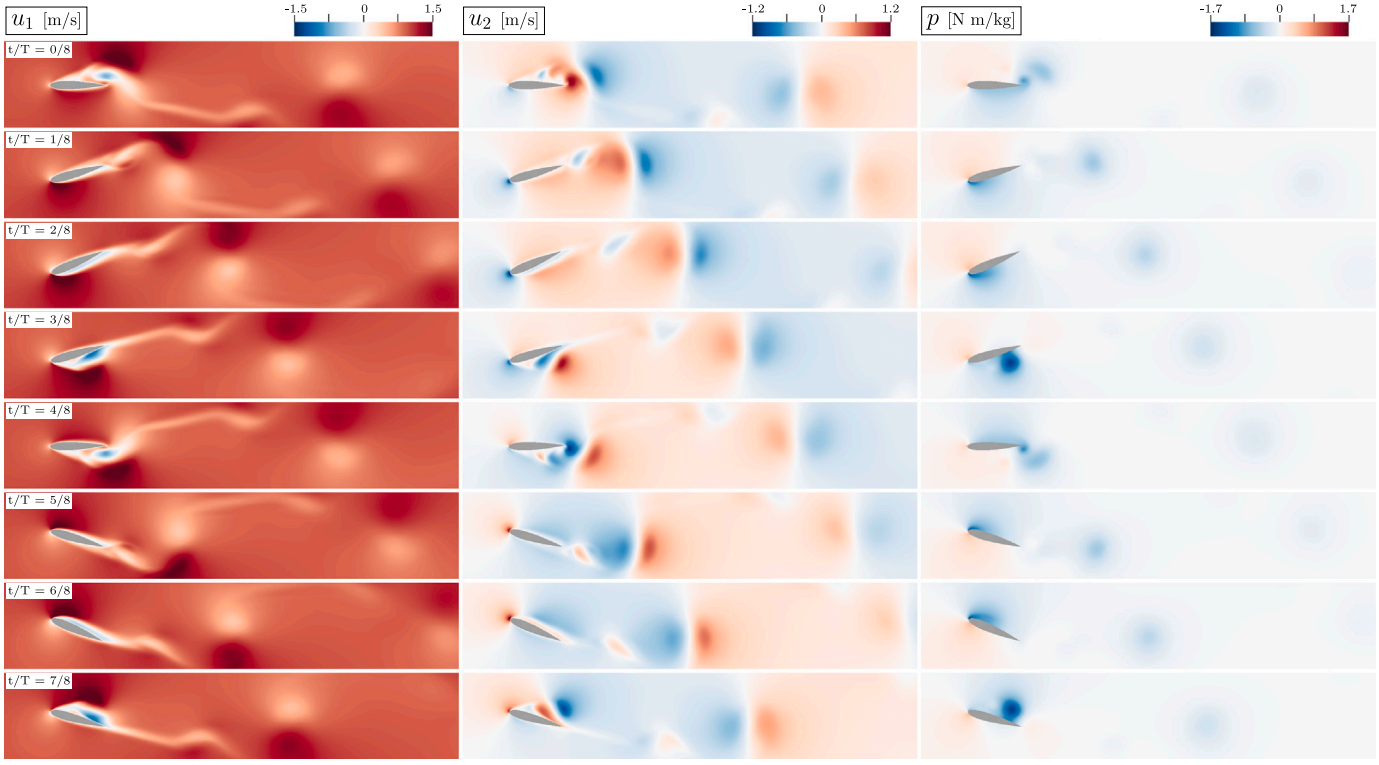

Fig. 10. Velocity and pressure plots of a pitching hydrofoil with an angle of 23° and a period $T = 8.33$ s for 8 moments in time. $\mathbb{R}e = 1100$.

the conservation properties of the formulation and use a conservative traction evaluation. Numerical experiments on flow past stationary and moving hydrofoils demonstrate very good accuracy, even on coarse meshes. The computed drag and lift coefficients match with results from the literature and history effects in the wake are accurately captured.

We outline two possible further research directions. First, the computational setup should be extended to three spatial dimensions (i.e. the corresponding boundary value problem is four-dimensional). Second, exploring the benefits of the computational setup in the reduced order modeling context could yield various advantages. The transformation of the time-dependent problem into a boundary value problem might allow for faster and more accurate evaluation of reduced order models for periodic flows.

CRediT authorship contribution statement

Jacob E. Lotz: Conceptualization, Data curation, Investigation, Methodology, Software, Validation, Visualization, Writing – original draft, Writing – review & editing. **Marco F.P. ten Eikelder:** Conceptualization, Methodology, Supervision, Writing – original draft, Writing – review & editing. **Ido Akkerman:** Conceptualization, Methodology, Funding acquisition, Project administration, Software, Supervision, Writing – original draft.

Declaration of competing interest

The authors declare that they have no known competing financial interests or personal relationships that could have appeared to influence the work reported in this paper.

Data availability

Data will be made available on request.

Acknowledgments

This publication is part of the project Lift Control for Hydrofoil Craft (with project number TWM. BL.019.009) of the research programm Top Sector Water & Maritime: The Blue Route which is (partly) financed by the Dutch Research Council (NWO), The Netherlands. This support is gratefully acknowledged. MtE acknowledges support from the German Research Foundation (Deutsche Forschungsgemeinschaft DFG) via the Walter Benjamin project EI 1210/1-1. The authors are grateful for the valuable criticism of the anonymous reviewers which has improved the clarity and quality of paper.

References

[1] Johnson AA, Tezduyar TE. Mesh update strategies in parallel finite element computations of flow problems with moving boundaries and interfaces. Comput Methods Appl Mech Engrg 1994;119:73–94.
[2] Michelassi V, Wissink JG, Rodi W. Direct numerical simulation, large eddy simulation and unsteady Reynolds-averaged Navier-Stokes simulations of periodic unsteady flow in a low-pressure turbine cascade: A comparison. Proc Inst Mech Eng A: J Power Energy 2003;217(4):403–12.
[3] Kinsey T, Dumas G. Parametric study of an oscillating airfoil in a power-extraction regime. AIAA J 2008;46(6):1318–30.
[4] Fried I. Finite-element analysis of time-dependent phenomena. AIAA J 1969;7(6):1170–3.
[5] Oden JT. A general theory of finite elements. I. Topological considerations. Internat J Numer Methods Engrg 1969;1(2):205–21.
[6] Oden JT. A general theory of finite elements. II. Applications. Internat J Numer Methods Engrg 1969;1(3):247–59.
[7] Mittal S, Tezduyar TE. Notes on the stabilized space-time finite-element formulation of unsteady incompressible flows. Comput Phys Comm 1992;73(1–3):93–112.
[8] Tezduyar TE, Aliabadi SK, Behr M, Johnson A, Mittal S. Parallel finite-element computation of 3D flows. Computer 1993;26:27–36.
[9] Tezduyar TE, Aliabadi SK, Behr M, Mittal S. Massively parallel finite element simulation of compressible and incompressible flows. Comput Methods Appl Mech Engrg 1994;119:157–77.
[10] Hughes TJR, Franca LP, Hulbert GM. A new finite element formulation for computational fluid dynamics: VIII. The Galerkin/least-squares method for advective-diffusive equations. Comput Methods Appl Mech Engrg 1989;73(2):173–89.
[11] Shakib F, Hughes TJR. A new finite element formulation for computational fluid dynamics: IX. Fourier analysis of space-time Galerkin/least-squares algorithms. Comput Methods Appl Mech Engrg 1991;87(1):35–58.
[12] Masud A, Hughes TJR. A space-time Galerkin/least-squares finite element formulation of the Navier-Stokes equations for moving domain problems. Comput Methods Appl Mech Engrg 1997;146(1–2):91–126.
[13] Tezduyar TE, Behr M, Liou J. A new strategy for finite element computations involving moving boundaries and interfaces-The deforming-spatial-domain / space-time procedure: I. The concept and the preliminary numerical tests. Comput Methods Appl Mech Engrg 1992;94:339–51.
[14] Tezduyar TE, Behr M, Mittal S, Liou J. A new strategy for finite element computations involving moving boundaries and interfaces-The deforming-spatial-domain / space-time procedure: II, Computation of free-surface flows, two-liquid flows, and flows with drifting cylinders. Comput Methods Appl Mech Engrg 1992;94:353–71.
[15] Mittal S, Tezduyar TE. A finite element study of incompressible flows past oscillating cylinders and aerofoils. Internat J Numer Methods Fluids 1992;15:1073–118.
[16] Mittal S, Tezduyar TE. Massively parallel finite element computation incompressible flows involving fluid-body interactions. Comput Methods Appl Mech Engrg 1994;112:253–82.
[17] Hughes TJR. Multiscale phenomena: Green's functions, the Dirichlet-to-Neumann formulation, subgrid scale models, bubbles and the origins of stabilized methods. Comput Methods Appl Mech Engrg 1995;127(1–4):387–401.
[18] Hughes TJR, Feijóo GR, Mazzei L, Quincy J. The variational multiscale method—a paradigm for computational mechanics. Comput Methods Appl Mech Engrg 1998;166(1–2):3–24.
[19] Hughes TJR, Stewart JR. A space-time formulation for multiscale phenomena. J Comput Appl Math 1996;74(1–2):217–29.
[20] Bazilevs Y, Calo VM, Cottrell JA, Hughes TJR, Reali A, Scovazzi G. Variational multiscale residual-based turbulence modeling for large eddy simulation of incompressible flows. Comput Methods Appl Mech Engrg 2007;197(1–4):173–201.
[21] Bazilevs Y, Michler C, Calo VM, Hughes TJR. Weak Dirichlet boundary conditions for wall-bounded turbulent flows. Comput Methods Appl Mech Engrg 2007;196(49–52):4853–62.
[22] Stoter SKF, ten Eikelder MFP, de Prenter F, Akkerman I, van Brummelen EH, Verhoosel CV, Schillinger D. Nitsche's method as a variational multiscale formulation and a resulting boundary layer fine-scale model. Comput Methods Appl Mech Engrg 2021;382:113878.
[23] Codina R. Stabilized finite element approximation of transient incompressible flows using orthogonal subscales. Comput Methods Appl Mech Engrg 2002;191(39–40):4295–321.
[24] ten Eikelder MFP, Akkerman I. Correct energy evolution of stabilized formulations: The relation between VMS, SUPG and GLS via dynamic orthogonal small-scales and isogeometric analysis. II: The incompressible Navier-Stokes equations. Comput Methods Appl Mech Engrg 2018;340:1135–59.
[25] Evans JA, Kamensky D, Bazilevs Y. Variational multiscale modeling with discretely divergence-free subscales. Comput Math Appl 2020;80(11):2517–37.
[26] ten Eikelder MFP, Bazilevs Y, Akkerman I. A theoretical framework for discontinuity capturing: Joining variational multiscale analysis and variation entropy theory. Comput Methods Appl Mech Engrg 2020;359:112664.
[27] ten Eikelder MFP, Akkerman I. Variation entropy: a continuous local generalization of the TVD property using entropy principles. Comput Methods Appl Mech Engrg 2019;355:261–83.
[28] Hughes TJR, Cottrell JA, Bazilevs Y. Isogeometric analysis: CAD, finite elements, NURBS, exact geometry and mesh refinement. Comput Methods Appl Mech Engrg 2005;194(39–41):4135–95.
[29] Cottrell JA, Hughes TJR, Bazilevs Y. Isogeometric analysis: toward integration of CAD and FEA. John Wiley & Sons; 2009.
[30] Otoguro Y, Takizawa K, Tezduyar TE. Space–time VMS computational flow analysis with isogeometric discretization and a general-purpose NURBS mesh generation method. Comput & Fluids 2017;158:189–200.
[31] Kuraishi T, Takizawa K, Tezduyar TE. Space-time isogeometric flow analysis with built-in Reynolds-equation limit. Math Models Methods Appl Sci 2019;29:871–904.
[32] Montardini M, Negri M, Sangalli G, Tani M. Space–time least–squares isogeometric method and efficient solver for parabolic problems. Math Comp 2020;89(323):1193–227.
[33] Saadé C, Lejeunes S, Eyheramendy D, Saad R. Space-time isogeometric analysis for linear and non-linear elastodynamics. Comput Struct 2021;254:106594.
[34] Takizawa K, Tezduyar TE. Multiscale space-time fluid-structure interaction techniques. Comput Mech 2011;48(3):247–67.
[35] Takizawa K, Henicke B, Puntel A, Spielman T, Tezduyar TE. Space-time computational techniques for the aerodynamics of flapping wings. J Appl Mech 2012;79:1–10.
[36] Takizawa K, Tezduyar TE. Space-time computation techniques with continuous representation in time (ST-C). Comput Mech 2014;53(1):91–9.
[37] Tezduyar TE, Takizawa K. Space–time computations in practical engineering applications: a summary of the 25-year history. Comput Mech 2019;63(4):747–53.
[38] Takizawa K, Tezduyar TE. Space-time fluid-structure interaction methods. Math Models Methods Appl Sci 2012;22:1–49.
[39] Gupta VK, Bhatu SK. Solution of cyclic profiles in catalytic reactor operation with periodic flow reversal. Comput Chem Eng 1991;15:229–37.
[40] Salinger AG, Eigenberger G. The direct calculation of period states of the reversible flow reactor - I. Methodology and propane combustion results. Chem Eng Sci 1996;51:4903–13.
[41] Bazilevs Y, Akkerman I. Large eddy simulation of turbulent Taylor–Couette flow using isogeometric analysis and the residual-based variational multiscale method. J Comput Phys 2010;229(9):3402–14.
[42] Kelley CT, Keyes DE. Convergence analysis of pseudo-transient continuation. SIAM J Numer Anal 1998;35(2):508–23.
[43] Coffey TS, Kelley CT, Keyes DE. Pseudotransient continuation and differential-algebraic equations. SIAM J Sci Comput 2003;25(2):553–69.
[44] Chorin AJ. A numerical method for solving incompressible viscous flow problems. J Comput Phys 1997;135(2):118–25.
[45] Chorin AJ. Numerical solution of the Navier-Stokes Equations. Math Comp 1968;22(104):745–62.
[46] Témam R. Sur l'approximation de la solution des équations de Navier-Stokes par la méthode des pas fractionnaires (I). Arch Ration Mech Anal 1969;32(2):135–53.
[47] Brooks AN, Hughes TJR. Streamline upwind/Petrov-Galerkin formulations for convection dominated flows with particular emphasis on the incompressible Navier-Stokes equations. Comput Methods Appl Mech Engrg 1982;21(1):199–259.

[48] Tezduyar TE, Mittal S, Ray SE, Shih R. Incompressible flow computations with stabilized bilinear and linear equal-order-interpolation velocity-pressure elements. Comput Methods Appl Mech Engrg 1992;95:221–42.
[49] Evans JA, Hughes TJR. Isogeometric divergence-conforming B-splines for the unsteady Navier-Stokes equations. J Comput Phys 2013;241:141–67.
[50] ten Eikelder MFP, Akkerman I. Correct energy evolution of stabilized formulations: The relation between VMS, SUPG and GLS via dynamic orthogonal small-scales and isogeometric analysis. I: The convective–diffusive context. Comput Methods Appl Mech Engrg 2018;331:259–80.
[51] Hughes TJR, Engel G, Mazzei L, Larson MG. The continuous Galerkin method is locally conservative. J Comput Phys 2000;163(2):467–88.
[52] Abbott IHA, Von Doenhoff AE. Theory of wing sections, including a summary of airfoil data. TA - TT -. Dover Publications; 1959.
[53] Behr M, Hastreiter D, Mittal S, Tezduyar TE. Incompressible flow past a circular cylinder: dependence of the computed flow field on the location of the lateral boundaries. Comput Methods Appl Mech Engrg 1995;123(1–4):309–16.
[54] Anderson R, Andrej J, Barker A, Bramwell J, Camier JS, Cerveny J, Dobrev V, Dudouit Y, Fisher A, Kolev T, Pazner W, Stowell M, Tomov V, Akkerman I, Dahm J, Medina D, Zampini S. MFEM: A modular finite element methods library. Comput Math Appl 2021;81:42–74.
[55] Drela M. XFOIL: An analysis and design system for low reynolds number airfoils. In: reynolds number aerodynamics Low, editor. Mueller, T.J.. Berlin, Heidelberg: Springer Berlin Heidelberg; 1989, p. 1–12.
[56] Kurtulus DF. On the unsteady behavior of the flow around NACA 0012 airfoil with steady external conditions at Re=1000. Int J Micro Air Veh 2015;7(3):301–26.
[57] Liu Y, Li K, Zhang J, Wang H, Liu L. Numerical bifurcation analysis of static stall of airfoil and dynamic stall under unsteady perturbation. Commun Nonlinear Sci Numer Simul 2012;17(8):3427–34.
[58] Khalid MSU, Akhtar I. Characteristics of flow past a symetric airfoil at low Reynolds number: a nonlinear perspective. In: Proceedings of IMECE2012. 2012, p. 167–75.
[59] Theodorsen T. General theory of aerodynamic instability and the mechanism of flutter. Technical report, Langley Memorial Aeronautical Laboratory; 1949, p. 26.